

# Angle-Selective Reflective Filters for Exclusion of Background Thermal Emission

Enas Sakr<sup>1,\*</sup> and Peter Bermel<sup>1,2</sup>

<sup>1</sup>*School of Electrical and Computer Engineering, Purdue University, West Lafayette, Indiana 47907, USA*

<sup>2</sup>*Birck Nanotechnology Center, Purdue University, West Lafayette, Indiana 47907, USA*

(Received 1 December 2016; revised manuscript received 21 February 2017; published 24 April 2017)

Selective filtering of spectral and angular optical transmission has recently attracted a great deal of interest. While optical passband and stop-band spectral filters are already widely used, angle-selective transmission and reflection filtering represents a less than fully explored alternative. Nonetheless, this approach can be promising for several applications, including stray radiation minimization and background emission exclusion. In this work, a concept for angle-selective reflection filtering using guided-mode resonance coupling is proposed. Although guided-mode resonance structures are already used for spectral filtering, in this work, a variation of angle-selective reflection filtering using guided-mode resonance coupling is proposed. We investigate angle-dependent properties of such structures for potential use as angle-selective reflective filters. We utilize interference between diffraction modes to provide tunable selectivity with a sufficient angular width. Combining these structures with thermal emitters can exclude selected emission angles for spatially selective thermal emissivity reduction toward sensitive targets, as well as directionally selective emissivity exclusion for suppression of solar heating. We show a very large selective reduction of heat exchange by 99.77% between an engineered emitter and a distant receiver using just a single-groove grating and an emitting substrate in the emitter's side. Also, we show a selective reduction of heat exchange by approximately 77% between an emitter covered by engineered sets of angle-selective reflective filters and a nearby sensitive target. The suggested angle-selective structure may have applications in excluding background thermal radiation, in particular, thermal emission reduction for daytime radiative cooling, sensitive IR telescope detectors, and high-fidelity thermoluminescent spectroscopy.

DOI: [10.1103/PhysRevApplied.7.044020](https://doi.org/10.1103/PhysRevApplied.7.044020)

## I. INTRODUCTION

Controlling the angular selectivity of optical transmission is a recently emerging branch of photonics, which has recently attracted a great deal of interest [1–5]. With recent advances in nanophotonics, broadband angular selectivity has recently been achieved in the laboratory. Some examples include microscale compound parabolic concentrators to limit the emission angle for solar cells [1,6], nonresonant Brewster modes in metallic gratings for angle-selective broadband absorption and selective thermal emission [7], and 1D photonic crystal heterostructures [8,9]. This approach can also allow for significant reduction of unwanted optical noise over a wide frequency range [4].

These examples show that selective angular *transmission* is well established. However, a tunable angle-selective *reflection* peak has not been demonstrated yet. In fact, Babinet's principle indicates that it should generally be possible to achieve such a goal through processes such as inversion [10]. Such an approach can be useful for elimination of unwanted optical components from a certain direction, for example, to mitigate optical noise effects from a known source. However, achieving this goal

requires a methodology to fully control directional angular *reflection* peaks or transmission *nulls*, exactly like a notch filter in the spatial angular domain.

In this work, we present a methodology to design arbitrary control of angular selectivity using reflection resonances. We propose guided-mode resonance (GMR) filters [11] to provide this functionality, using high-contrast dielectric gratings (HCGs) [12] or, more generally, photonic crystal slabs [13,14]. The resonant selective behavior of GMR filters results from interference of resonances in the high-index decorated slab with the background transmission and manifests itself as a Fano-resonance line shape [13]. It has been shown that GMR modes strongly depend on the incident angle on the slab and polarization [15]. Thus, they can provide tunability over incident angles and wavelengths. Also, the angular properties of wideband GMR reflectors has been theoretically and experimentally demonstrated recently [16]. Since GMR modes experience both index guiding and photonic band-gap confinement, their associated quality factors are usually high [11,15]. It is also possible to modify their behavior by controlling coupling to multiple diffraction modes. The physics can be understood through the framework of the coupled-mode theory [17], where a resonant mode can have different decay channels according to the associated loss mechanisms. For example, if the GMR filter is suspended in air,

\*Corresponding author.  
esakr@purdue.edu

there will be two decay channels in the forms of reflection and transmission at the two surfaces of the slab. When the number of decay channels increases due to the presence of multiple diffraction orders, the quality factor decreases. Hence, it is possible to control the angular width, as well as the resonance frequency quality factor based on this argument. Moreover, these loss rates control the resonant-mode amplitude [18]. Controlling the coupling parameters and loss rates can be achieved mainly by controlling the geometry of the GMR filter, primarily the lateral period of the structure and the thickness of the slab.

We show simple structures based on GMR filters that exhibit the selective reflection angular property over a given frequency range. The simplest example is a single-groove HCG for a given incident light polarization. In our previous work [19], we show that this HCG can be designed to exhibit reflection angular selectivity around the normal direction. The mechanism depends on destructive interference at the exit of the slab, despite the presence of the resonant mode. In this paper, we propose double-groove HCG for larger tunability of guided-mode resonances over incident angles. We also place a low-loss absorber as a substrate and use GMR filters to control absorptivity and emissivity as implied by Kirchhoff's law of thermal radiation [20]. Consequently, GMR filters can be used for spatial control of thermal emission *nulls*, where a specific region on a receiver admits reduced emissivity. The chosen design of the double-groove grating allows for a lower quality factor and wider angular widths of the emission nulls and, hence, provides flexibility for designing thermal emitters and receivers.

One of the applications that may benefit from reflection angular selectivity is daytime radiative cooling [21,22], a passive process in which the cooling power increases rapidly with the temperature. To avoid counterproductive heating by sunlight that cancels out this beneficial cooling effect, a solar-blind thermal emitter is needed. Also, angle-selective reflective filters can be useful to reduce or eliminate noise from nearby thermal emitters in sensitive optical detectors. One example is stray thermal emission in IR telescopes that limits the signal-to-noise ratio (SNR) due to unavoidable emission from the telescope structure itself [23]. In certain cases, optical filters and traditional cooling approaches can help [24,25], but there are limits to the performance that can be achieved with this approach. Higher SNRs can be achieved by engineering angle-selective reduction of thermal emissivity to suppress unwanted thermal emission at the detector, while maintaining sufficient thermal emission elsewhere to keep important components at acceptable temperatures.

Another example where stray thermal emission limits the detection of optical signals is thermoluminescent spectroscopy (TLS) [26–28] for dosimetry and aging. In TLS systems, when a luminophor is heated, it is provided with sufficient thermal energy to release a metastable state that

emits electromagnetic radiation. If the emitted optical signal is weak or is near red wavelengths, it may be very difficult to detect amidst blackbody radiation from heaters [28–30]. Several methods to reduce blackbody radiation noise from heaters include using lock-in amplifiers [31], photon counting [32], differential measurements to subtract blackbody contribution [27], and minimizing the exposed heater area [29], as well as employing low-emissivity selective heater structures [30]. These result in significant improvements in the detection of certain luminophors, but the detection of weaker TL emission and/or in the presence of stronger background signals (e.g., at high temperatures or longer wavelengths) can benefit from less noisy detection. Therefore, angle-selective thermal emission reduction can also be employed in conjunction with spectrally selective approaches to minimize thermal emission towards optical components from exposed heater surfaces.

While there has already been a great deal of work to design spectrally and directionally selective thermal emitters within a narrow range of wavelengths and angles [33–35], there is still an opportunity to investigate the complementary design, i.e., directionally selective emission *nulls*. However, previous concepts for altering angular reflectivity require anisotropic dependence of the permittivity to enhance reflection in one direction [36]. Unfortunately, anisotropic permittivity is not available naturally. Alternatively, resonant reflection filters can provide angular selectivity with simple structures and simultaneously include spectral selectivity around the resonance frequency.

First, the physics of GMR filters is discussed to show its eligibility for angle-selective reflection control. Then we utilize the concept of GMR filters to reduce thermal emission or absorption towards a distant target. The proposed thermal emitter reduces energy exchange with the far target in a specific frequency range by designing a directional emission or absorption null in the normal direction. This approach can be useful for daytime radiative cooling through the rejection of heat absorption from the normal direction where the direct component of sunlight is received.

More generally, for nearby emitting sources, for example, the structural support of an IR telescope, we present an engineered design of a thermal emitter that spatially excludes the emitted power towards a vulnerable target on the receiver, e.g., the IR detector, for a given range of emitted wavelengths. In this study, we assume a quasi-2D problem, in which an emitter surface has infinite length in one direction and a finite length  $l_1$  in the other direction. The receiver is also infinite in one direction and is of the same length as the emitter  $l_1 = l_2$  in the same direction. The emitter and receiver planes are separated by a distance  $D$ . As shown in Fig. 1, the region of length  $l_r$  is placed in the middle of the receiver's plane, where the sensitive component is located. Whether the emitter is distant or close to the receiver is defined by whether or not  $D \gg l_1$ . If it is not distant, the emitter is segmented in  $N$  sections, each

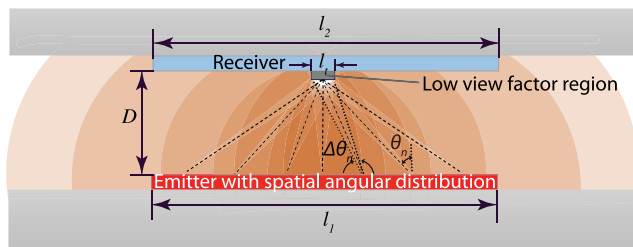


FIG. 1. Angular thermal emission exclusion. Emitter and receiver of equal widths  $l_1 = l_2$  and infinite extension in the perpendicular direction are separated by a distance  $D$ . To reduce the power received at the target (center area of the receiver), a set of directionally selective segments is placed over the emitter's surface so that each segment excludes the emission from its center towards the target's center. The exclusion angular width should be reduced as the distance between the segment and the target increases.

of which has a null emission towards the target at an angle  $\theta_n$ , where  $n$  is the segment's index that changes from zero at the center to a maximum value determined based on the emitter's length  $l_1$  and the separation distance  $D$ . The angular width  $\Delta\theta_n$  decreases gradually from the center to the sides of the emitter. In this way, radiation is prohibited towards and around the center and allowed elsewhere.

## II. METHODS

The emissivity function depends on the wavelength, angle, and polarization. To compute the emissivity function, we use Kirchhoff's law of thermal radiation [20], which states that the absorptivity equals the emissivity for a given wavelength, angle, and polarization in thermal equilibrium. Hence, it is possible to compute the emissivity dependence with the wavelength, angle, and polarization through a reflection and transmission analysis. Hence, based on Kirchhoff's law, we can think that a directional null of the emissivity means a directional null in the absorptivity, or if the structure does not allow transmission of incident waves, then a directional null of absorptivity means a directional maximum of reflectivity. This method simplifies the requirements of this study, since the problem is now reduced to the angular modification of reflectivity. Therefore, a filter with the desired angular dependence can be used on top of a low-loss thick absorber or emitter. In the remainder of this section, we summarize our approach to precisely calculate the band structure, absorptivity, and view factor for specific structures.

### A. Band-structure computation

The  $p$ -polarization guided-mode resonances are radiative modes guided in the grating structure. To compute the locations of these modes, harmonic inversion of time signals [37] as implemented in MEEP, a freely available finite-difference time-domain code [38], is used to extract

resonance frequencies and their associated quality factors. The computational cell consists of a unit cell of the GMR on a semi-infinite substrate of permittivity 2.1. This simulation is two dimensional, since the structure has infinite extent in one direction. The boundary conditions of the computational cell are periodic Bloch boundary conditions on the sides of the unit cell, with a varying parallel  $k$  vector to span values of  $k_x$  from 0 to  $0.5(2\pi/a)$ . Perfectly matching layers are also placed on the top and the bottom of the computational cell as boundary conditions of the semi-infinite layers. A Gaussian magnetic current source oriented in the  $y$  direction, as shown below in Fig. 2(a), is placed in the air above the grating to excite  $p$ -polarized resonant modes.

### B. Absorptivity computation

Rigorous coupled-wave analysis (RCWA) combined with the  $S$ -matrix algorithm implemented in the Stanford Stratified Structure Simulator (S4) [39] is used to perform the absorptivity calculation. The unit cell of the absorbing or emitting structure consists of five layers: the semi-infinite air, Si grating, low-loss thick absorber, an ideal metallic back reflector with permittivity of  $-50$ , and a semi-infinite air bottom layer. To obtain reliable results, the number of in-plane Fourier modes [39] is set to 30, which gives acceptable accuracy of the results and does not show a big difference when the number increases. For each incident angle, the reflectivity  $R$  is computed for the designated range of frequencies, then the absorptivity  $A$  is  $1 - R$ . Figure 2(c) is obtained with a constant permittivity value set to  $2.1 + 0.005i$ , while the results in Fig. 3 are obtained using a permittivity value with real part of 2.1 and imaginary part adapted from the absorption coefficient in Ref. [40] for Yb-doped glass optical dispersion data. The assumption is valid as long as the absorption coefficient is low enough not to violate the Kramers-Kronig relation.

### C. View factor calculation

The view factor  $F_{1-2}$  allows us to quantify the strength of the thermal exchange and is defined as the probability that a thermal photon emitted by one surface  $A_1$  is received by another surface  $A_2$ . It is generally given by [41]

$$F_{1-2} = \frac{1}{A_1} \int dA_1 \int dA_2 \frac{\cos\theta_1 \cos\theta_2}{\pi r^2}, \quad (1)$$

where the angles  $\theta_1$  and  $\theta_2$  are the angles between the surface normal to infinitesimal areas  $dA_1$  and  $dA_2$ , respectively, and the line connecting them whose length is  $r$ .

Symbolic integration of a related expression [19] with respect to  $y$  yields a closed-form expression, which can be generalized to incorporate wavelength- and angle-dependent emissivities. The resulting wavelength-dependent view factor  $F_{1-2}(\lambda)$  is then given by

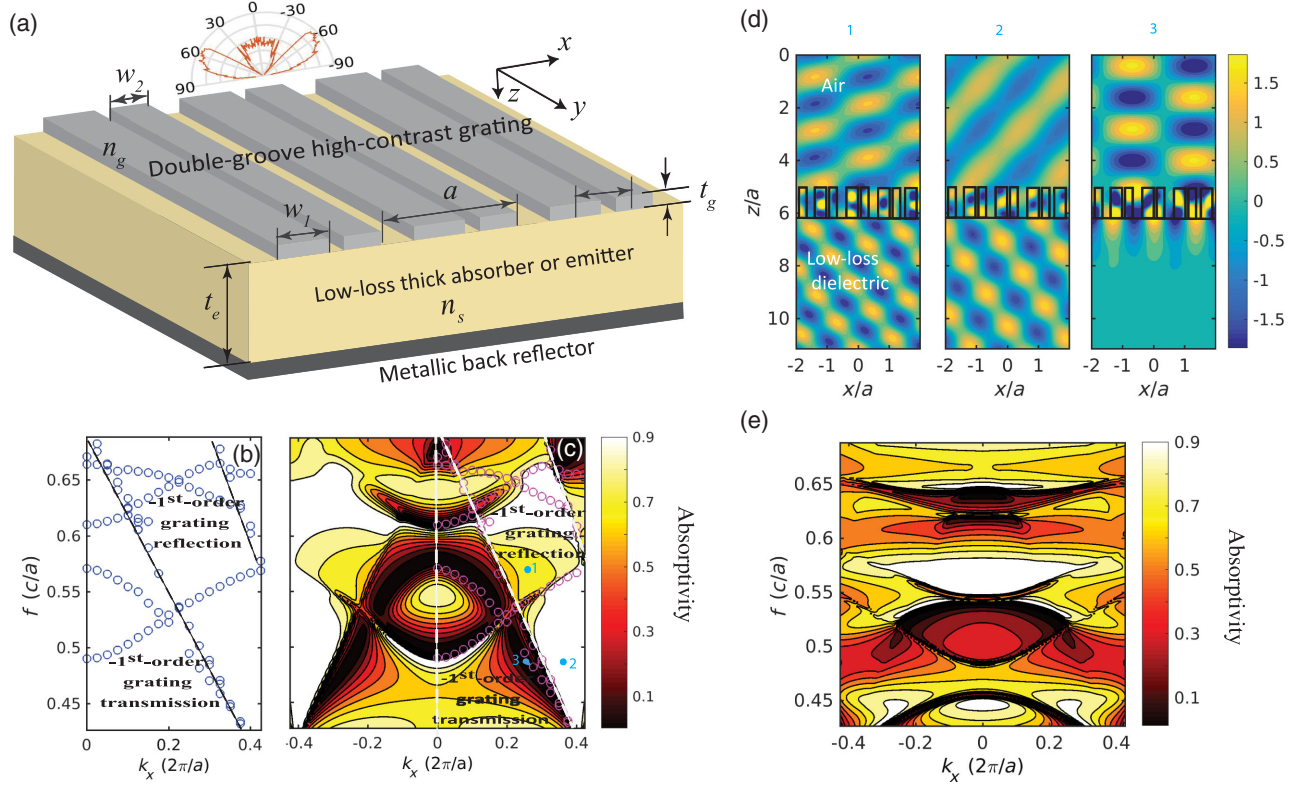


FIG. 2. (a) Angular exclusion emitter segment. The segment consists of a low-loss absorbing or emitting substrate and a metallic back reflector. A selective GMR filter or a HCG is placed on top. The value of the period  $a$  is chosen to select a specific angular exclusion band for a given wavelength. (b) Band structure of a Si double-groove grating with a *lossless* transparent substrate computed using MEEP HARMINV. The detected modes are reflection or transmission resonance peaks. (c) The computed absorption for different incident angles and frequencies. Normalized units are used to compare the transmission with the band structure. The band structure is plotted in magenta to compare the computed bands in (b) with the absorption spectra. In (b) and (c), the dashed lines are  $-1$ st-order transmission and reflection modes, respectively.  $w_1$  and  $w_2$  are assumed to be  $0.335a$  and  $0.2235a$ , respectively, separated by a distance of  $0.4022a$ . The grating thickness  $t_g$  is  $1.15a$ . (d) Field profiles at three different points on (c): (1) Resonant coupling to zeroth-order reflection and zeroth- and  $-1$ st-order transmission, (2) resonant coupling to zeroth- and  $-1$ st transmission, and (3) resonant coupling to zeroth-order reflection. (e) Absorption spectra of  $s$ -polarized modes showing that polarization dependence is crucial for 1D grating structures.

$$F_{1-2}(\lambda) = \frac{\int_{x_1=-l_1/2}^{l_1/2} dx_1 \int_{x_2=-l_2/2}^{l_2/2} dx_2 \{ \epsilon(\lambda, x_1, x_2) f(D, x_1, x_2) \}}{\int_{x_1=-l_1/2}^{l_1/2} dx_1 \int_{x_2=-\infty}^{\infty} dx_2 \{ \epsilon(\lambda, x_1, x_2) f(D, x_1, x_2) \}}, \quad (2)$$

where  $f(D, x_1, x_2) = 0.5D^2 / (D^2 + x_1^2 - 2x_1x_2 + x_2^2)^{3/2}$ , and  $l_1$ ,  $l_2$ , and  $D$  are the emitter's length, the receiver's length, and the separation distance between their centers, respectively. Note that the receiver's length can be the target's length  $l_t$  only or the length of the receiver excluding the target, depending on which view factor we seek. In the latter case, the integration in the numerator is broken into a summation of two integrals spanning  $x_2 = -l_2/2$  to  $-l_t/2$ , and  $x_2 = l_t/2$  to  $l_2/2$ . To transform all the computations to Cartesian coordinates  $x_1$  and  $x_2$ , the emissivity function  $\epsilon(\lambda, x_1, x_2)$  is extracted from the wavelength- and angle-dependent emissivity  $\epsilon(\lambda, \theta)$  obtained from S4 simulations

and transformed via  $\tan\theta = (x_1 - x_2)/D$  where the origins  $x_1 = 0$  and  $x_2 = 0$  are placed in the middle of the emitter and the middle of the receiver, respectively. The view factor computed using the above expression is validated against standard closed-form values in Ref. [41] for different test cases of an ideal blackbody emitter and receiver at different separation distances. Photon-recycling effects are neglected.

### III. RESULTS AND DISCUSSION

#### A. Photonic design for angular exclusion

To demonstrate angular exclusion, we seek angular reflection filters that couple all incident light into reflection modes at a given wavelength, with a sufficient angular width to cover a target location. Accordingly, we propose a design based on Si HCGs, assuming that Si is thermally transparent in the wavelength range of interest. As shown in Fig. 2(a), it is a double-groove grating with a refractive

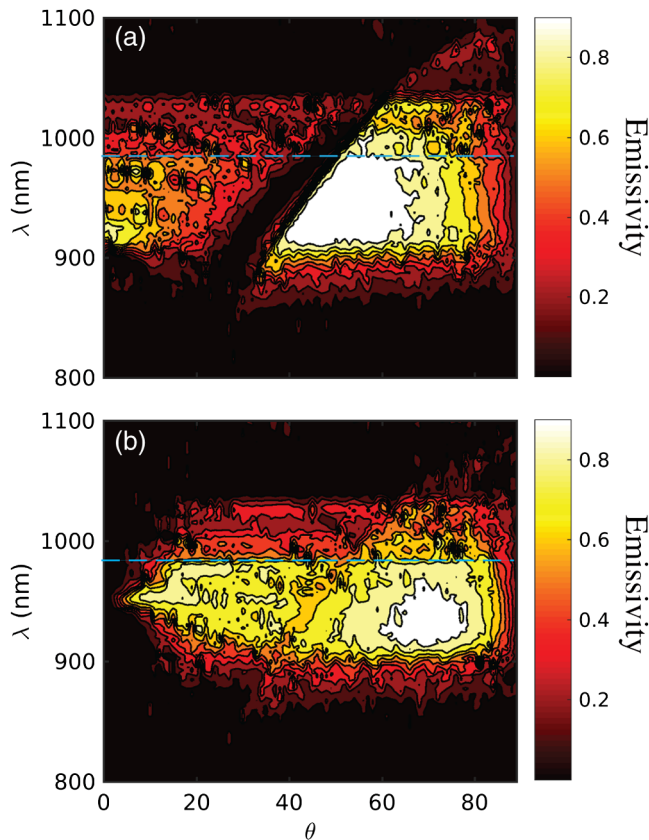


FIG. 3. Two examples of emissivity contour plots for an emitter with a Yb-doped substrate as a frequency-selective substrate. (a) Emissivity plot of the thermal emitter in Fig. 2(a), with period  $a = 440$  nm. Changing  $a$  steers the null angle, specifically at 982.5 nm (dashed blue line). (b) Emissivity plot of a structure similar to Fig. 2(a) but with a single-groove grating (as described in Ref. [19]). The grating thickness is  $0.6a$ , and the Si filling factor is  $0.68a$ , where  $a = 454.3$  nm. An emitter segment with emissivity spectra in (b) is used for the middle segment [number 6 in Fig. 5(a)].

index  $n_g$  with period  $a$ , and thickness  $t_g$ , with two ridges of widths  $w_1$  and  $w_2$  separated by distance  $d$ . We utilize the design parameters employed in Ref. [42] scaled for our target angles and wavelengths. In previous work, a single-groove grating was used for emission prohibition in the normal direction [19]. Here, a *double-groove* HCG filter is chosen because it shows a wide range of tunability of angular exclusion and asymmetry at key wavelengths. For the purpose of tailoring thermal emission, we put the GMR filter on a low-loss absorbing substrate, which can be a piece of *transparent* ceramic or glass with low absorption coefficient. The substrate also can be doped with rare-earth dopants as a method to provide frequency selectivity [43,44]. Also, a metallic back reflector is placed on the bottom of the substrate to ensure full absorption within a single reflection. Multiple reflections, however, may cause different behavior, since the design depends on full transmission, and eventually full absorption occurs in the low-loss thick ceramic substrate.

To assess the dispersion properties of the double-groove HCG, resonant-mode analysis is carried out as described in Sec. II using harmonic inversion [37] (HARMINV) available through MEEP [38]. The computed  $p$ -polarization band structure for a HCG with  $n_g = 3.49$  and a *lossless semi-infinite* substrate with refractive index  $n_s = 1.45$  is shown in Fig. 2(b). The HCG thickness is set to  $t_g = 1.15a$  with ridge dimensions of  $0.2235a$  and  $0.335a$ , respectively, separated by a distance  $d = 0.4022a$ . It is important to mention that all the detected modes are radiation modes, and they will be resonating inside the HCG and radiating energy to the surrounding media. In the dispersion characteristics, the onset of subsequent propagating diffraction modes is clearly evident. These are marked by the black dashed lines in Fig. 2(b). The first line marks the onset of the  $-1$ st grating *transmission* mode defined by  $k_x = k_{xs} - k_G$ , where  $k_x$  is the wave vector in air,  $k_{xs}$  is the maximum propagating wave vector in the transparent substrate, and  $k_G$  is an integer multiple of momentum added by the grating lattice primitive vector ( $2\pi/a$ ). The second line marks the onset of the  $-1$ st *reflection* mode defined by  $k_x = k_{x0} - k_G$ , where  $k_{x0}$  is the maximum propagating wave vector in air. The detected resonance peaks are either reflection or transmission modes based on the phase difference between the resonant mode and the background reflection or transmission of the substrate. In terms of the coupled-mode theory, the detected resonant modes are a result of intermode coupling between the involved diffraction modes. Since the substrate is lossless in this modal analysis, the loss mechanisms are purely radiative. The diffraction channels involved are the zeroth-order reflection and transmission and the  $-1$ st transmission below the first dashed line, above which the  $-1$ st reflection appears.

To compute the response of the HCG filter on an absorbing substrate, we use the structure shown in Fig. 2(a) with an absorbing substrate of sufficiently large thickness  $t_e$  with  $n_s = 1.45 + 0.0017i$  to represent silica glass with impurities. The  $p$ -polarized absorptivity is computed at different incident angles and frequencies using RCWA and the  $S$ -matrix algorithm implemented in S4 [39] as explained in Sec. II. A contour plot of the computed absorptivity is shown in Fig. 2(c). The diffraction-mode edges are also evident in Fig. 2(c), and a match between the resonant absorption dips and the band structure in Fig. 2(b) occurs where the resonance is primarily reflective. We also notice an asymmetric response above the  $-1$ st reflection line for positive and negative incident angles. This asymmetry indicates the difference of the phase profile of the surface implied by the nonsymmetric geometry of the double-groove HCG [42]. It is worth mentioning that this asymmetric absorption does not appear before the onset of the  $-1$ st reflection mode. The reason is that only the zeroth-order reflection is present, and regardless of the asymmetry of the coupling to the available diffraction modes in the substrate, the accumulated phases at the exit of the grating

to air will be the same. Accordingly, the sum of the diffracted waves in the substrate is similar if a wave is incident from the right or the left sides. Efficient coupling to the  $-1$ st reflection from this HCG and the asymmetric behavior is discussed in detail in Ref. [42]. Although the direction of the scattered fields does not affect emissivity, the scattering direction makes a great deal of difference when designing an angle-selective reflective filter, since the flow of the scattered transmission may be important to deliver power to subsequent layers. Careful grating design is needed to prevent power splitting between diffraction modes.

To better understand the interference between different diffraction modes, we present the parallel magnetic field profile  $H_y$  at different points on the absorptivity plot in Fig. 2(c). We choose three points with considerably different field profiles and plot them in Fig. 2(d).

- (a) The first case shows a mode that couples incident radiation to both the transmitted and reflected modes [incident angle =  $31^\circ$  at  $k_x = 0.295(2\pi/a)$  and  $f = 0.5728c/a$ ]. The field pattern in air shows interference between the incident wave and the zeroth-order reflection, since the  $-1$ st reflection is not yet supported. The transmitted field pattern in the low-loss dielectric shows interference between the zeroth-order transmission and the  $-1$ st-order transmission modes.
- (b) The second case shows a mode that couples the incident mode to transmission modes (incident angle =  $52^\circ$  at  $k_x = 0.3833(2\pi/a)$  and  $f = 0.486c/a$ ). The transmitted field pattern in the low-loss dielectric shows interference between the zeroth-order transmission and  $-1$ st-order transmission modes.
- (c) The third case shows a mode that couples all incident radiation to reflection modes (incident angle =  $31^\circ$  at  $k_x = 0.2505(2\pi/a)$  and  $f = 0.486c/a$ ). The field pattern in air shows interference between the incident wave and the zeroth-order reflection, since the  $-1$ st reflection is not yet supported.

Finally, the proposed design is effective only with the  $p$ -polarized component of stray thermal radiation. To show the significant dependence on the polarization state, we plot the absorptivity spectra for  $s$ -polarized incident plane waves in Fig. 2(e). It shows that the resonant modes are significantly different from the  $p$ -polarized resonant modes. However, it is still possible to use a polarization filter at the target to screen out the  $s$ -polarized incident radiation. Another possible solution is to consider polarization-independent GMR filters, for example, by using 2D structures [45,46] or by engineering the GMR filter such that the  $s$ - and  $p$ -polarized resonant modes match at a single frequency [47]. It is also important to emphasize that the GMR filter material selection is arbitrary as long as the reflection directional resonances can be tuned for the different emitter segments.

## B. Frequency selectivity and segments design

For the design depicted in Fig. 1, each emitter segment should have a spatially dependent emission null; thus, it is necessary to modify the angular dependence of the emissivity function for each segment. The contour plot of Fig. 2(c) is the basis of the design of the individual emitter's segments. One can choose an arbitrary null angle and select the corresponding normalized frequency from which a value of the period  $a$  can be selected. To constrain the spectral response, we choose a frequency-selective doped transparent substrate. We assume a Yb-doped glass as a frequency-selective emitting substrate, with a peak absorption coefficient around 950 nm. The frequency-selective absorption coefficient "masks" the contour plot in Fig. 2(c) and selects only a band of frequencies with some angular dispersion. An example is plotted in Fig. 3(a) with the value of  $a = 440.26$  nm. In designing the segments, the period is chosen such that the selective frequency band is in the range of normalized frequencies between  $0.4$  and  $0.5c/a$ , to exclude emission in a single direction while avoiding unnecessary elimination of emission in other directions, at a given wavelength. Another advantage of choosing the absorption nulls in this normalized frequency range is that the angular width of the null direction decreases for larger angles, which fulfills the original requirement of the emitter design as described in Fig. 1.

To assemble the emitting setup described in Fig. 1, the emitter is first divided into  $N = 11$  segments, with the minimum and maximum null angles  $\theta_1 = -48^\circ$  and  $\theta_{11} = 48^\circ$ . We then pick a specific wavelength for which the received power should be reduced. In this example, we choose 982.5 nm [marked by the blue dashed lines in Figs. 3(a) and 3(b)]. We prepare five sets of simulations to gradually change the angle from approximately  $48^\circ$  to  $10^\circ$ , for segments 1 through 5 and for segments 11 through 7, as shown in Fig. 5(a). For the middle segment (number 6), we utilize the emitter design described in our previous work [19], in which a similar design to Fig. 2(a) was introduced but with using a *single-groove* Si HCG instead with grating thickness of  $0.6a$  and ridge width of  $0.68a$ , where  $a = 454.3$  nm. The emissivity spectra of this middle segment at different incident angles with a Yb-doped substrate are shown in the contour plot of Fig. 3(b).

## C. View factor reduction

In this section, we present two cases of view factor reduction. We first study the view factor reduction due to using GMR filters for a distant receiver situation. Second, we study the view factor reduction due to a spatially dependent angle selective thermal emitter close to the receiver.

### 1. A distant emitter and receiver

We start with the simpler case where the receiver is far away. For this purpose, it is required to reduce the heat

exchange in the normal direction only. Thus, the emitter is covered with a single-grating structure whose emissivity spectrum is shown in Fig. 4(a). The obtained spectrum ignores the substrate's dispersion and absorption. We consider two scenarios to model this situation. The first scenario assumes that the emitter is radiating directly in the normal direction, similar to the emission received from the direct component of sunlight. The receiver is a thick, transparent, *nonselective*, low-loss absorbing substrate covered with a single-groove GMR of period

$a = 872.64$  nm. We assume that the emitter and the receiver have the same width  $l$  and are separated by a distance  $D = 0.5l$ . This scenario mimics a daytime radiative cooling setting, where heat exchange is prevented from the normal direction and allowed otherwise. To calculate the reduction of the received power at the target, we compute the view factor with the proposed design and compare it to the view factor obtained for a blackbody at the same temperature and with the same dimensions and separation distance. The normalized view factor plotted in Fig. 4(b) is the ratio between the former and the latter view factors. A large reduction in the normalized view factor over a wide range of wavelengths (1500 to 2200 nm) that reaches more than 99% around 1530 and 2130 nm is evident in Fig. 4(b).

In the second scenario, we consider an emitter with a *frequency-selective* substrate with emissivity spectra shown in Fig. 3(b). The receiver is assumed to have no angular dependence. We study the effect of changing the separation distance  $D$ . The separation distance should be large enough so that the angular width dispersion eliminates radiation received from different locations on the emitter. The minimum separation distance may be estimated as  $D_{\min} = l_t/[2 \tan(\Delta\theta/2)]$ , where  $l_t$  is the target's length, and  $\Delta\theta$  is the angular spread around the normal direction as described in Fig. 4(a). Increasing the separation distance above  $D_{\min}$  will further reduce the received power at the target compared to a blackbody emitter at the same wavelength. The normalized view factor is plotted in Fig. 4(c), assuming an emitter of length  $l_1 = l$  and a target of length  $l_t = 0.5l$ , while the separation distance  $D$  is varied from  $l_1$  to  $5l_1$ . In Fig. 4(c), we notice that the expected view factor reduction becomes more pronounced at larger separation distances. The reduction of thermal power reaching the target is at least 99% for  $\lambda = 977.5$  nm when  $D > D_{\min}$ .

## 2. A nearby receiver

In the second case where the emitter is close to the receiver, the design in Fig. 1 can be useful, given a proper design. To realize this concept, one can think of the emitter as a set of individual point sources radiating thermal power with tailored angular emission patterns, such that a null is available at the target's direction. In this way, we can arrange adjacent emitter segments so that each segment will act as an emitter point source with a null radiation towards the target, while the emission lobes deliver power to the rest of the receiver's surface. In the ideal situation, the null directions and the angular widths of the null points change adiabatically between segments, according to the separation distance between the specific segment and the receiver and the dimensions of the protected target. If the segment is not small enough, then nonconforming emission nulls will contribute substantially more emission at the target.

For that purpose, we consider an example for the emitter design as shown in Fig. 5(a), where arbitrary emitting

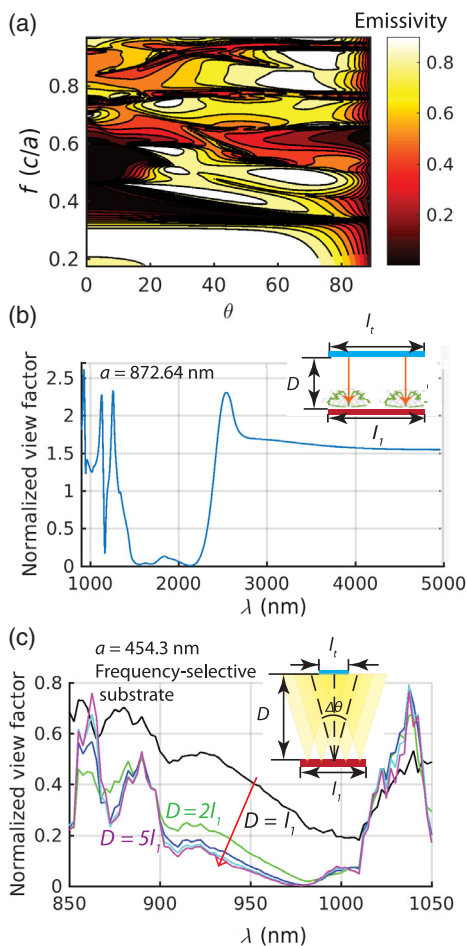


FIG. 4. (a) Emissivity contour plot of an emitter composed of a transparent low-absorbing substrate and a single-groove grating GMR filter. (b) The view factor reduction (99.77%) expected between a directional emitter separated by a distance  $D = 0.5l$  from a receiver with emissivity spectra plotted in (a). The design setup depicted in the inset mimics heat exchange with the direct component of the Sun. (c) The computed reduction of the view factor between a distant target receiver of length  $0.5l$  at a distance  $D$  from an emitter of length  $l_1$  (inset). The whole emitter's surface is covered with a single-groove GMR filter with spectra plotted in Fig. 3(b), where a frequency-selective absorptive substrate is used. Yellow beams in the inset depict the range of *excluded* angles. The normalized view factor is plotted for separation distances of  $l_1$ ,  $2l_1$ ,  $3l_1$ ,  $4l_1$ , and  $5l_1$ . For  $D > l_1$ , the reduction is 99.77% at 977.5 nm.

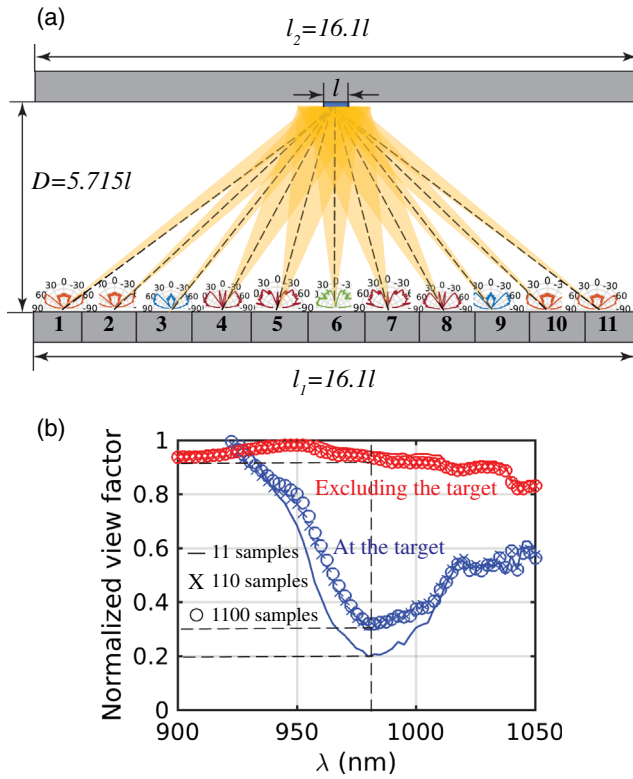


FIG. 5. (a) Achieving angular exclusion with 11 emitter segments. The emission pattern of each segment is plotted at 982.5 nm. Yellow beams depict the range of *excluded* angles to reduce the view factor at the target. (b) The computed normalized view factor at the target (red) and over the receiver’s surface (blue). The computed view factor is normalized by the original view factor for each surface without exclusion. Sampling more emitting sources over each segment increases the received power at the target because of the increased overlap between different emitting sources over each segment.

segments can be arranged to give emission nulls at the target as we discussed earlier. The emission pattern of each segment is plotted, and the shaded yellow areas show the null direction and their angular extension over the target. As shown in Fig. 5(a), the target length is  $l$  and the emitter and the receiver are of the same length  $l_1 = l_2 = 1.61l$ , while the separation distance  $D$  is  $5.75l$ . Note that the segment’s length should be large enough to include a sufficient number of periods of the HCG to avoid reduction of the resonant peaks’ amplitudes, as well as spectral broadening [48]. The view factor is computed as described in Ref. [41] but for a surface with infinite extension in one direction (see Sec. II). The obtained view factor is plotted in Fig. 5(b) but normalized to the value of the view factor in the absence of any angular shaping emitters. Ideally, we expect to see a dip to zero of the normalized view factor around the design wavelength of 982.5 nm. Although the normalized view factor does not go to zero at 982.5, it still shows a dip at this particular wavelength, with a reduction of almost 80%, compared to a plane blackbody emitter. This nonzero received power at the target is mainly caused

by the null angular width being insufficient to cover the whole target area, as well as the residual emission at each null. Consequently, further optimization of the designed segments can provide better overlap of nulls at the target. We also notice that the normalized view factor is below 70% for wavelengths between 950 and 1010 nm, which is simply due to the dispersion characteristics of the emission nulls that still keep the received power at the target sufficiently low, despite the fact that the nulls are displaced at these wavelengths.

Another source of extra emission in a real device is the fact that each line segment over the emitter surface will act as a line thermal source; thus, it makes sense to sample a number of points over each segment during the view factor calculation to mimic a realistic situation. Since these sampled sources will not have the exact overlap with the target due to their spatial offset from the center of the segment, it is expected that these extra sources will contribute more power at the target. The expected reduction of the normalized view factor is also plotted in Fig. 5(b), and it shows that ten samples over each segment are enough to describe the realistic response for this example, since similar results are obtained with 100 sampling sources for each segment. Of course, with these extra sources added, the normalized view factor decreases reduction to almost 69% at 982.5 nm.

To show that the received power decreases only at the target, we perform the same calculations of the view factor over the rest of the receiver’s surface. The computed view factor plotted also in Fig. 5(b) in red shows a reduction of only 6.6% at 982.5 nm caused mainly by the presence of mirror symmetric null of each segment at the opposite directions of the target. Accordingly, the proposed design can selectively exclude the emission towards a target without a significant alteration of the power flow to the surrounding areas.

As mentioned earlier, the emission reduction is best when properties of emitter segments vary adiabatically across the surface. In the case of a finite number of fabricated emitter segments with distinct properties, it is possible to estimate the contribution of each segment to the received power at the target and then identify the biggest contributors and replace them by a better matching of emission patterns. The contour plots in Figs. 6(a) and 6(b) show the received power from each emitter segment at the target and over the receiver’s surface excluding the target, respectively, over the selective range of wavelengths. First, we note that the values of the received power in Fig. 6(a) are one order of magnitude less than Fig. 6(b). This behavior is expected since the target’s area is much less than the receiver’s area. Second, the received power over the range of wavelengths from 970 to 1010 nm [Fig. 6(a)] is greatly reduced if compared to the received power over the shorter wavelengths. Third, if we plot the received power from each segment of the emitter at 982.5 nm [inset of Fig. 6(a)], we notice that there are some locations where the received



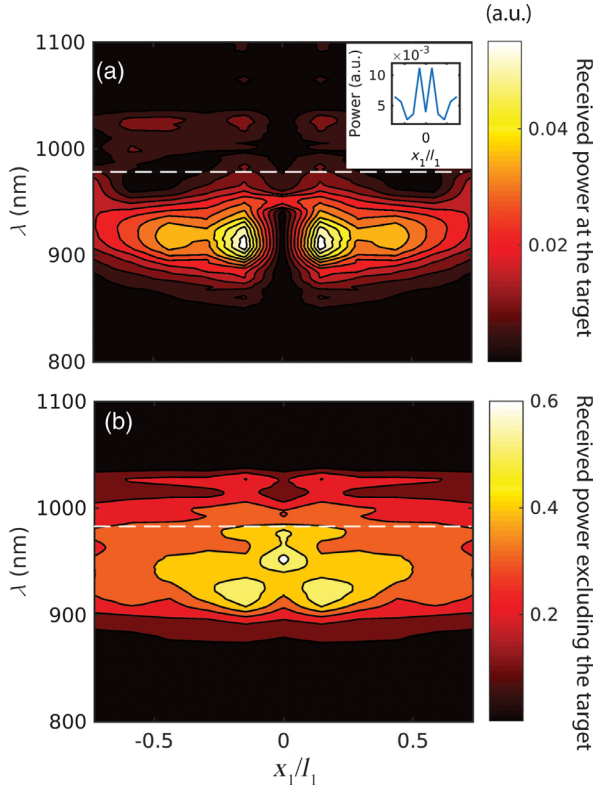


FIG. 6. (a) The received power at the target from each emitter segment. At the target wavelength, the closest emitter segments to the receiver show high received power, suggesting an optimization for these segments (inset). (b) The received power over the rest of the receiver's surface. High values of power are received keeping the total view factor sufficiently high.

power is large. This suggests replacing these elements, especially those closer to the center of the emitter, indexed by 5, 6, and 7 in Fig. 5(a), with emitting elements showing larger angular spread around the null direction. Specifically, we replace them with emission patterns extracted from Fig. 3(b), to give wider coverage over the target's surface. Upon replacing elements 5, 6, and 7, we obtain an increased reduction of the view factor as shown in Fig. 7(c), with received power plotted in Figs. 7(a) and 7(b). The inset of Fig. 7(a) shows the reduction of the power emitted specifically from the middle segments compared to the inset of Fig. 6(a). Although replacing these elements contributes to a better view factor reduction (77% in this case), the replaced segments, however, cause some reduction of the received power at the surface excluding the target to 9.9% compared to 6.6% in Fig. 5(b). Fortunately, the decreased view factor outside the target is not significant, since substantial power is still received from other emitter segments. Although this modification does not provide a 100% reduction of the view factor at the target, further numerical optimization of the GMR filters on each emitter segment can also be utilized to push the angular emissivity reduction at the target to near 100%. In future

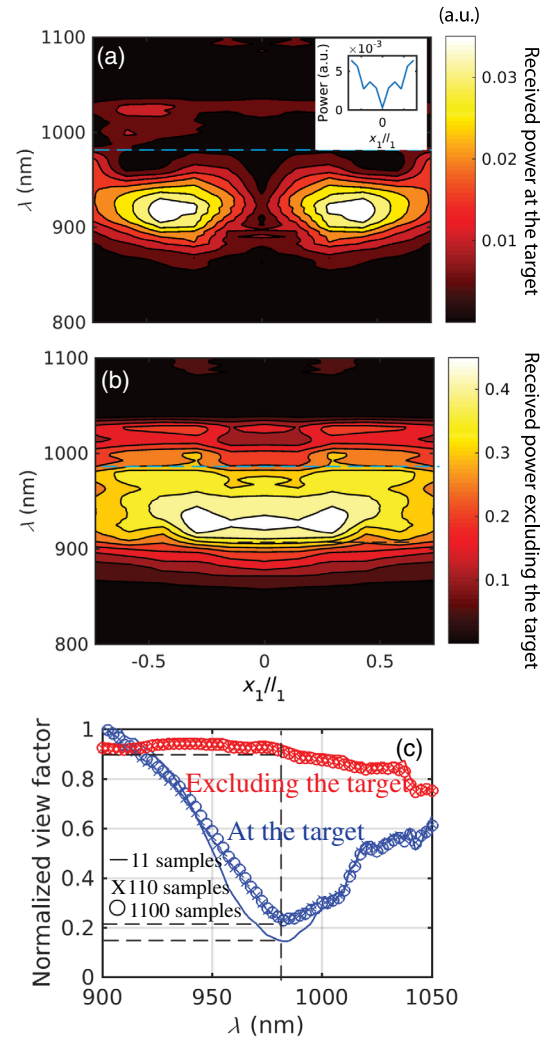


FIG. 7. (a) and (b) are the same as Fig. 6 but after replacing three emitter segments. The received power from these segments reduces compared to Fig. 6 (inset). (c) Improvement of the view factor after replacing the center segments. The normalized view factor at the target is reduced to 0.23 (77% reduction) of its original value; however, the total view factor over the rest of the surface is reduced to 0.91 (<10% reduction) of its original value.

work, one may consider steering nulls into a targeted solid angle through a 2D periodic surface array of emitter elements.

#### IV. CONCLUSION

We propose a photonic structure based on guided-mode resonance filters on thick low-loss emitters for narrowband directional thermal emission exclusion to reduce thermal exchange between a distant receiver and an emitter or a nearby emitter and a sensitive target. For a distant emitter, a reduction of 99.77% is shown using a single-groove HCG grating eliminating emission in the normal direction, which can operate over either a narrow or broad range of wavelengths. For a nearby thermal emitter, the reflection

resonances of the GMR filters are tuned almost adiabatically over the emitter's surface to yield a radiation null at the target. Frequency selectivity can be achieved using a frequency-selective emitter substrate, such as a rare-earth-doped glass. Careful tailoring of emitter segments shows a view factor reduction at the target of approximately 77% compared to a relatively minor (<10%) view factor reduction over other areas around the target. While this design focuses on a single wavelength, it may be extended to a broader band. Finally, this approach may find applications in daytime radiative cooling, stray radiation reduction in IR telescopes, and thermoluminescence spectroscopy.

### ACKNOWLEDGMENTS

The authors thank Deanna Dimonte and Shailja Dhaka for providing code that was used in the preparation of this manuscript. The authors also thank Justus Ndukaife for providing valuable feedback on the manuscript. Support is provided by the Department of Energy, under DOE Cooperative Agreement No. DEEE0004946 (PVMi Bay Area PV Consortium), the NEC Corporation, Northrop Grumman Aerospace Systems in support of "Infrared metasurfaces for redirecting light and managing thermal emission," and the NSF Grant No. EEC 1454315-CAREER: Thermophotonics for Efficient Harvesting of Waste Heat as Electricity. The computational resources for this work are provided by the Network of Computational Nanotechnology under NSF Grant No. EEC-0228390.

- 
- [1] E. D. Kosten, J. H. Atwater, J. Parsons, A. Polman, and H. A. Atwater, Highly efficient GaAs solar cells by limiting light emission angle, *Light Sci. Appl.* **2**, e45 (2013).
- [2] E. D. Kosten, B. M. Kayes, and H. A. Atwater, Experimental demonstration of enhanced photon recycling in angle-restricted GaAs solar cells, *Energy Environ. Sci.* **7**, 1907 (2014).
- [3] S. V. Boriskina *et al.*, Roadmap on optical energy conversion, *J. Opt.* **18**, 073004 (2016).
- [4] Y. Shen, C. W. Hsu, Y. X. Yeng, J. D. Joannopoulos, and M. Soljačić, Broadband angular selectivity of light at the nanoscale: Progress, applications, and outlook, *Appl. Phys. Rev.* **3**, 011103 (2016).
- [5] Y. Xu, T. Gong, and J. N. Munday, The generalized Shockley-Queisser limit for nanostructured solar cells, *Sci. Rep.* **5**, 13536 (2015).
- [6] J. H. Atwater, P. Spinelli, E. Kosten, J. Parsons, C. Van Lare, J. Van de Groep, J. Garcia de Abajo, A. Polman, and H. A. Atwater, Microphotonic parabolic light directors fabricated by two-photon lithography, *Appl. Phys. Lett.* **99**, 151113 (2011).
- [7] C. Argyropoulos, K. Q. Le, N. Mattiucci, G. D'Aguanno, and A. Alù, Broadband absorbers and selective emitters based on plasmonic Brewster metasurfaces, *Phys. Rev. B* **87**, 205112 (2013).
- [8] Y. Shen, D. Ye, I. Celanovic, S. G. Johnson, J. D. Joannopoulos, and M. Soljačić, Optical broadband angular selectivity, *Science* **343**, 1499 (2014).
- [9] Y. Shen, D. Ye, L. Wang, I. Celanovic, L. Ran, J. D. Joannopoulos, and M. Soljacic, Metamaterial broadband angular selectivity, *Phys. Rev. B* **90**, 125422 (2014).
- [10] X. Ni, S. Ishii, A. V. Kildishev, and V. M. Shalaev, Ultra-thin, planar, Babinet-inverted plasmonic metalenses, *Light Sci. Appl.* **2**, e72 (2013).
- [11] S. S. Wang and R. Magnusson, Theory and applications of guided-mode resonance filters, *Appl. Opt.* **32**, 2606 (1993).
- [12] V. Karagodsky, F. G. Sedgwick, and C. J. Chang-Hasnain, Theoretical analysis of subwavelength high contrast grating reflectors, *Opt. Express* **18**, 16973 (2010).
- [13] S. Fan and J. D. Joannopoulos, Analysis of guided resonances in photonic crystal slabs, *Phys. Rev. B* **65**, 235112 (2002).
- [14] J. D. Joannopoulos, S. G. Johnson, J. N. Winn, and R. D. Meade, *Photonic Crystals: Molding the Flow of Light*, 2nd ed. (Princeton University, Princeton, NJ, 2008).
- [15] J. Song, R. Proietti Zaccaria, M. B. Yu, and X. W. Sun, Tunable Fano resonance in photonic crystal slabs, *Opt. Express* **14**, 8812 (2006).
- [16] Y. H. Ko, M. Niraula, K. J. Lee, and R. Magnusson, Properties of wideband resonant reflectors under fully conical light incidence, *Opt. Express* **24**, 4542 (2016).
- [17] W. Suh, Z. Wang, and S. Fan, Temporal coupled-mode theory and the presence of non-orthogonal modes in lossless multimode cavities, *IEEE J. Quantum Electron.* **40**, 1511 (2004).
- [18] M. Ghebrebrhan, P. Bermel, Y. X. Yeng, I. Celanovic, M. Soljacic, and J. D. Joannopoulos, Tailoring thermal emission via  $Q$  matching of photonic crystal resonances, *Phys. Rev. A* **83**, 033810 (2011).
- [19] E. Sakr, D. Dimonte, and P. Bermel, Metasurfaces with Fano resonances for directionally selective thermal emission, *MRS Adv.* **1**, 3307 (2016).
- [20] S. E. Han, Theory of thermal emission from periodic structures, *Phys. Rev. B* **80**, 155108 (2009).
- [21] A. P. Raman, M. A. Anoma, L. Zhu, E. Rephaeli, and S. Fan, Passive radiative cooling below ambient air temperature under direct sunlight, *Nature (London)* **515**, 540 (2014).
- [22] T. Safi and J. Munday, Improving photovoltaic performance through radiative cooling in both terrestrial and extraterrestrial environments, *Opt. Express* **23**, A1120 (2015).
- [23] M. S. Strojnik, Stray-light issues for background-limited far-infrared telescope operation, *Opt. Eng. (Bellingham, Wash.)* **33**, 681 (1994).
- [24] P. Bouchet *et al.* The mid-infrared instrument for the James Webb Space Telescope, III: MIRIM, the MIRI Imager, *Publ. Astron. Soc. Pac.* **127**, 612 (2015).
- [25] P. A. R. Ade *et al.*, BICEP2. II. Experiment and three-year data set, *Astrophys. J.* **792**, 62 (2014).
- [26] H. E. Prescott, J. R. Fox, P. J. Akber, and R. A. Jensen, Thermoluminescence emission spectrometer, *Appl. Opt.* **27**, 3496 (1988).
- [27] E. P. Manche, Differential thermoluminescence (DTL)—A new instrument for measurement of thermoluminescence with suppression of blackbody radiation, *Rev. Sci. Instrum.* **49**, 715 (1978).

- [28] W. M. Burch, Thermoluminescence, low radiation dosage and black-body radiation, *Phys. Med. Biol.* **12**, 523 (1967).
- [29] T. Hashimoto, An overview of red-thermoluminescence (RTL) studies on heated quartz and RTL application to dosimetry and dating, *Geochronometria* **30**, 9 (2008).
- [30] P. R. Armstrong, M. L. Mah, K. D. Olson, L. N. Taylor, and J. J. Talghader, Reduction of thermal emission background in high temperature microheaters, *J. Micromech. Microeng.* **26**, 055004 (2016).
- [31] J. Lippert and V. Mejdahl, Thermoluminescence readout instrument for measurement of small doses, Proc. Int. Conf. Luminescence Dosim., USAEC CONF-650637 (1967).
- [32] G. M. Hieftje, Signal-to-noise enhancement through instrumental techniques. II. Signal averaging, boxcar integration, and correlation techniques, *Anal. Chem.* **44**, 69A (1972).
- [33] D. Costantini, A. Lefebvre, A.-L. Coutrot, I. Moldovan-Doyen, J.-P. Hugonin, S. Boutami, F. Marquier, H. Benisty, and J.-J. Greffet, Plasmonic Metasurface for Directional and Frequency-Selective Thermal Emission, *Phys. Rev. Applied* **4**, 014023 (2015).
- [34] G. Biener, N. Dahan, A. Niv, V. Kleiner, and E. Hasman, Highly coherent thermal emission obtained by plasmonic bandgap structures, *Appl. Phys. Lett.* **92**, 081913 (2008).
- [35] M. De Zoysa, T. Asano, K. Mochizuki, A. Oskooi, T. Inoue, and S. Noda, Conversion of broadband to narrowband thermal emission through energy recycling, *Nat. Photonics* **6**, 535 (2012).
- [36] F. Aieta, P. Genevet, N. Yu, M. A. Kats, Z. Gaburro, and F. Capasso, Out-of-plane reflection and refraction of light by anisotropic optical antenna metasurfaces with phase discontinuities, *Nano Lett.* **12**, 1702 (2012).
- [37] V. A. Mandelshtam and H. S. Taylor, Harmonic inversion of time signals and its applications, *J. Chem. Phys.* **107**, 6756 (1997).
- [38] A. F. Oskooi, D. Roundy, M. Ibanescu, P. Bermel, J. D. Joannopoulos, and S. G. Johnson, MEEP: A flexible free-software package for electromagnetic simulations by the FDTD method, *Comput. Phys. Commun.* **181**, 687 (2010).
- [39] V. Liu and S. Fan, S4: A free electromagnetic solver for layered periodic structures, *Comput. Phys. Commun.* **183**, 2233 (2012).
- [40] E. S. de L. Filho, G. Nemova, S. Loranger, and R. Kashyap, Laser-induced cooling of a Yb:YAG crystal in air at atmospheric pressure, *Opt. Express* **21**, 24711 (2013).
- [41] M. F. Modest, *Radiative Heat Transfer* (Academic Press, New York, 2013).
- [42] K. Ito and H. Iizuka, Highly efficient -1st-order reflection in Littrow mounted dielectric double-groove grating, *AIP Adv.* **3**, 062119 (2013).
- [43] D. Chubb, A. Pal, M. Patton, and P. Jenkins, Rare earth doped high temperature ceramic selective emitters, *J. Eur. Ceram. Soc.* **19**, 2551 (1999).
- [44] E. Sakr, Z. Zhou, and P. Bermel, Enhancing selectivity of infrared emitters through quality-factor matching, *Proc. SPIE Int. Soc. Opt. Eng.* **9608**, 960819 (2015).
- [45] E. Sakat, G. Vincent, P. Ghenuche, N. Bardou, C. Dupuis, S. Collin, F. Pardo, R. Haïdar, and J.-L. Pelouard, Free-standing guided-mode resonance band-pass filters: From 1D to 2D structures, *Opt. Express* **20**, 13082 (2012).
- [46] S. Peng and G. M. Morris, Resonant scattering from two-dimensional gratings, *J. Opt. Soc. Am. A* **13**, 993 (1996).
- [47] H. Xu-Hui, G. Ke, S. Tian-Yu, and W. Dong-Min, Polarization-independent guided-mode resonance filters under oblique incidence, *Chin. Phys. Lett.* **27**, 074211 (2010).
- [48] R. R. Boye and R. K. Kostuk, Investigation of the effect of finite grating size on the performance of guided-mode resonance filters, *Appl. Opt.* **39**, 3649 (2000).